RESEARCH ARTICLE | MAY 26 2026

Gradient-based optimization of scatterer arrangements based on the T-matrix method

N. Asadova ; J. D. Fischbach ; R. Vallée ; O. Kuster ; Y. Augenstein ; D. Vovchuk ; A. Kharchevskii ; P. Ginzburg ; C. Rockstuhl

APL Photonics 11, 056116 (2026)
https://doi.org/10.1063/5.0316808

Gradient-based optimization of scatterer arrangements based on the T-matrix method

Cite as: APL Photon. 11, 056116 (2026); doi: 10.1063/5.0316808
Submitted: 15 December 2025 • Accepted: 17 April 2026 •
Published Online: 26 May 2026

View Online Export Citation CrossMark

N. Asadova,[1,a] J. D. Fischbach,[1] R. Vallée,[2] O. Kuster,[3] Y. Augenstein,[4] D. Vovchuk,[5,6] A. Kharchevskii,[6] P. Ginzburg,[6] and C. Rockstuhl[1,3,7]

AFFILIATIONS

[1] Institute of Nanotechnology, Karlsruhe Institute of Technology (KIT), Karlsruhe, Germany
[2] Centre de Recherche Paul Pascal, University of Bordeaux, Pessac, France
[3] Institute of Theoretical Solid State Physics, Karlsruhe Institute of Technology (KIT), Karlsruhe, Germany
[4] Flexcompute Inc, Belmont, Massachusetts 02478, USA
[5] Institute of Photonics, Electronics and Telecommunications, Riga Technical University, Riga, Latvia
[6] School of Electrical Engineering, Tel Aviv University, Tel Aviv, Israel
[7] Center for Integrated Quantum Science and Technology (IQST), Karlsruhe Institute of Technology, Karlsruhe, Germany

[a] **Author to whom correspondence should be addressed:** nigar.asadova@kit.edu

ABSTRACT

The demand for inverse design is increasing as the ability to fabricate sub-10 nm features expands the design space significantly. Efficient inverse design benefits from differentiable models of light–matter interaction. While traditional full-wave solvers based on finite differences, finite elements, or Fourier modal methods have already been presented for that purpose, a dedicated tool adapted for performing multiple scattering simulations is still lacking. To overcome this limitation, we provide a multiple-scattering framework compatible to automatic differentiation, suitable for treating periodic and non-periodic arrangements of scatterers. It yields exact gradients regarding geometric and positional parameters in finite clusters and infinite metasurfaces. In this work, we use spheres as the building blocks to demonstrate the framework's capabilities as a standalone tool. However, the framework is adaptable to arbitrarily shaped scatterers, provided the individual T-matrices are calculated using differentiable Maxwell solvers. Since the gradients are obtained simultaneously in a single backward pass, the framework is well-suited for moderately dimensional problems. It is also possible to combine multiple performance goals into a single objective function. The versatility of our method is illustrated in proof-of-concept examples that focus on Kerker-type physics. In the first example, a finite cluster of scatterers is optimized in order to reach a high forward-to-backward scattering ratio and we show experimental feasibility of the designs. In the second example, a metasurface made from multiple scatterers per unit cell is designed to maximize the reflectance contrast between orthogonal linear polarizations of the incident light. We make the framework publicly available at https://github.com/tfp-photonics/dreams.

I. INTRODUCTION

With recent advances in the fabrication of nanophotonic devices, numerous design parameters can be tailored to achieve the desired optical response. This increase in degrees of freedom necessitates solving the inverse problem efficiently. In other words, we need to identify optimal design parameters so the nanophotonic device exhibits the desired optical response.

The most basic approach is to perform a parameter sweep and select the best performance among the calculated objective values. However, this quickly becomes infeasible with an increasing number of parameters, a phenomenon known as the curse of dimensionality. Therefore, over the decades, a plethora of more advanced approaches were introduced.[1–5] The problem to be solved within the framework of inverse design is to adjust each degree of freedom to reach the optimum for a desired objective function. Inverse

design employs various strategies such as deep learning,[6,7] topology optimization,[8–10] metaheuristic algorithms,[11–13] or probabilistic algorithms.[14,15]

However, scalability remains a critical challenge.[16,17] As the number of design parameters increases, the computational time required by heuristic methods often increases exponentially, making them less suitable for high-dimensional design problems.[18] Among different approaches, deep learning models provide practically immediate results after the training phase is completed. However, training depends on the availability of an extensive dataset. The data generation process scales exponentially with the dimensionality of the design space,[19] and in the majority of cases, each particular problem requires a dedicated training set. This renders such approaches computationally expensive in scenarios where the training data must be explicitly generated solely to train a neural network to solve a specific inverse design problem.

Therefore, in high-dimensional parameter spaces, gradient-based optimization methods are the primary choice for solving inverse problems. The known gradients provide the shortest path to a local optimum. Although the optimum is not global, the curse of dimensionality can become a blessing.[20] For very high-dimensional parameter spaces, the landscape is expected to flatten out such that the local maximum or minimum is close in value to the global one. However, this effect depends on the specific nature of the problem and must be empirically tested. Beyond the algorithmic considerations, it is also useful to understand the fundamental limits on what is achievable for a given material and design region.[21,22]

The calculation of gradients for complex computational code can be implemented in different ways. Numerical implementation with finite differences is typically not considered since it requires performing one additional simulation for each parameter variation. In the adjoint method, a second problem has to be manually formulated and solved and the solution provides the gradient of the objective function. It is usually formulated for PDE problems. The adjoint method is extensively used in density-based topology optimization, where each pixel or voxel in the device's elements serves as a degree of freedom.[23] This easily amounts to a total of 10^3–10^9 degrees of freedom. The resulting optimized shapes are free-form, and potential fabrication difficulties should be handled as well.[24–26]

An alternative approach to obtaining gradients is automatic differentiation (AD)—an automated approach that evaluates exact derivatives of a composition of elementary functions. As it is possible to spend the same amount of time to calculate the derivative with respect to all parameters, regardless of the number of parameters, a single optimization step takes roughly twice the time of a single simulation. Hybrid approaches replace manual derivation of the adjoint equation with AD.[27] However, fully differentiable implementations go further, re-implementing the solver entirely within the framework, with AD capabilities for ease of use and high performance.

Formulating tools for scientific computations in an automatically differentiable manner requires dedicated effort and careful implementation. In essence, every elementary function needs to be formulated as differentiable, something which poses challenges. Nevertheless, with the appreciation that gradient information is key to inverse design in high-dimensional parameter spaces, multiple efforts have been dedicated to formulating various methods that solve Maxwell's equations in an automatically differentiable manner. These include general-purpose full-wave Maxwell solvers, such as the finite-difference time-domain (FDTD) method,[28,29] and the finite element method (FEM).[30,31]

A special-purpose computational method that was already formulated in an automatically differentiable manner is the rigorous coupled-wave analysis (RCWA) method, also known as the Fourier modal method (FMM).[32,33] It has been extensively used within the AD framework[34–38] or adjoint method[39] and can be combined with topology optimization.[9–40] The discrete dipole approximation has also been used with an adjoint formulation for the optimization of multiple-scattering systems.[41] Another semi-analytical approach with a recently developed differentiable implementation is the hybrid coupled dipole method.[42] However, each of these automatically differentiable formulations inherits the pros and cons of the underlying computational method. Therefore, having a wide range of tools available that can be flexibly applied to specific problems is highly beneficial for further developing nanophotonics.

This contribution focuses on the automatic differentiation of a computational framework for nanophotonic scattering problems based on the T-matrix method. The benefit of the method lies in its semi-analytical treatment of the light–matter interaction with the elementary building blocks expressed using the T-matrix. The T-matrix captures how an incident field, expanded into vector spherical waves, is converted into a scattered field, which is also expanded into vector spherical waves. Once the T-matrix of an object is known, complex arrangements of many scatterers can be studied highly efficiently based on an underlying algebraic formulation. The scatterers can be arranged randomly or in a periodic pattern, forming metasurfaces or metamaterials. Such versatility renders the T-matrix applicable to a wide range of nanophotonic problems.[43–46] Our implementation follows the open-source *treams* package[47] and integrates AD capabilities into the multiscattering code.

A central milestone of our work is the development of a differentiable computational framework for calculating the optical response of complex arrangements of scatterers. The framework that we develop here enables differentiation with respect to input parameters, including not only the radii of individual spheres but also the positions of spheres or arbitrarily shaped scatterers in arrangements such as periodic arrays with complex unit cells containing multiple scatterers. Here, we use the term "moderately dimensional" to refer to optimization problems with approximately up to a hundred scatterers, with multipole truncation orders in the range $l_{\max} = 3$–7, which is sufficient for most of the nanophotonics problems. Depending on the parameterization, this corresponds to in the order of hundreds of optimizable variables.

Earlier implementations used analytically calculated derivatives of Mie coefficients, and the final derivatives were obtained using the adjoint method.[48,49] These studies did not utilize the AD framework, and the parameterization of scatterer positions was not integrated, as it requires more manual derivations. Recent publications applied gradient-free optimization to infinitely extended core-shell cylinders[50] and the arrangement of spheres.[51] Gradient-based optimization for chains of infinite cylinders was performed with Gaussian parameterization of positions.[52]

This article is structured as follows: In Sec. II, multiscattering formalism is introduced and the fundamentals of AD

are outlined. In Sec. III, an arrangement of spheres is optimized to achieve the maximum scattering ratio between the forward and backward hemispheres. Next, the optimization results for an example of a metasurface with a complex unit cell composed of spheres, optimized for polarization-selective reflectance, are discussed. By making the underlying Python source codes developed in this work publicly available on GitHub (https://github.com/tfp-photonics/dreams), we expect a substantial contribution to the further development of the field of nanophotonics that relies on scattering structures.

II. AUTOMATIC DIFFERENTIATION OF THE MULTISCATTERING FRAMEWORK

A. Multiscattering formalism

The T-matrix formalism is a versatile approach that simplifies the computation of the optical response for various arrangements of scatterers. Here, the T-matrix represents the linear relationship between expansion coefficients of the regular vector spherical waves that expand the incident field and the singular vector spherical waves that expand the scattered field,

$$\mathbf{p} = \mathbf{T}\,\mathbf{a}, \tag{1}$$

where $\mathbf{p}$ and $\mathbf{a}$ are vectors containing the expansion coefficients for the scattered field and the incident field, respectively,

$$\mathbf{E}_{\mathrm{inc}}(\mathbf{r},\omega) = \sum_{l=1}^{\infty}\sum_{m=-l}^{l}\left[a^{\mathrm{e}}_{lm}(\omega)\mathbf{N}^{(1)}_{lm}(\mathbf{r},\omega) + a^{\mathrm{m}}_{lm}(\omega)\mathbf{M}^{(1)}_{lm}(\mathbf{r},\omega)\right], \tag{2}$$

$$\mathbf{E}_{\mathrm{sca}}(\mathbf{r},\omega) = \sum_{l=1}^{\infty}\sum_{m=-l}^{l}\left[p^{\mathrm{e}}_{lm}(\omega)\mathbf{N}^{(3)}_{lm}(\mathbf{r},\omega) + p^{\mathrm{m}}_{lm}(\omega)\mathbf{M}^{(3)}_{lm}(\mathbf{r},\omega)\right]. \tag{3}$$

The fields are expanded in transverse electric (TE) and transverse magnetic (TM) vector spherical waves, $\mathbf{M}_{lm}(\mathbf{r},\omega)$ and $\mathbf{N}_{lm}(\mathbf{r},\omega)$. The superscripts correspond to regular (1) and singular (3) fields.[53] The T-matrix $\mathbf{T}$ represents the most comprehensive information on the linear optical response of a scatterer and can be obtained semi-analytically for basic objects, i.e., spheres and infinite cylinders, or numerically for arbitrarily shaped scatterers. The number of multipolar orders in the expansion can be truncated at a specific value, beyond which the contribution to the optical response can be considered negligible. This approach, therefore, offers clear advantages over the commonly used dipole approximation.

For arrangements of scatterers, a modified expression holds, which accounts for the contribution of the scattered field coming from other scatterers to the incident field on each scatterer,

$$\mathbf{p} = \left(\mathbb{1} - \mathbf{T}\mathbf{C}^{(3)}\right)^{-1}\mathbf{T}\mathbf{a}, \tag{4}$$

where $\mathbf{T}$ is a block-diagonal matrix, where each scatterer response is defined in its local coordinate system. All the translation coefficients are packed in the matrix $\mathbf{C}^{(3)}$, and $\mathbf{C}^{(3)}_{ij}$ depends on the distance from the j-th scatterer to the i-th scatterer. Please note that this is what we refer to as a local description, as each scatterer is represented by its T-matrix.

We can also employ a global T-matrix formulation, where the entire scattering response of an ensemble of scatterers is expressed relative to a specific origin.[54,55] This is beneficial since the T-matrix shrinks in size for problems with closely arranged scatterers. For the scattering problem of a periodic lattice, $\mathbf{C}^{(3)}_{ij}$ includes a sum over an infinite number of lattice sites. The direct evaluation of the sum converges poorly, so the Ewald method is employed.[56,57] By expanding the resulting T-matrix from the periodic spherical wave basis into the plane wave basis, the S-matrix of a single layer can be obtained, which relates the incoming and outgoing plane waves. Finally, the single infinite layer can be stacked with another two-dimensional lattice, an interface, or a homogeneous slab. Thus, the complete framework can simulate a diverse set of scattering arrangements.

B. Automatic differentiation

Now, with this framework, we can express the optical response of various types of photonic materials composed of an ensemble of isolated scatterers. However, for the inverse problem, we need to calculate the gradients, i.e., the change of an objective function derived from a forward simulation, depending on any of the degrees of freedom that we consider. To do so, we will automatically differentiate the code that solves the forward problem.

The basic idea of AD is to apply the chain rule to numerical values and not symbolic expressions. Consider $f\colon \mathbb{R}^m \to \mathbb{R}^n$ having m input values and n output values as a sequence of elementary operations. In an optimization task, the derivative of each output with respect to each input variable is required, which makes up a Jacobian of the size $n \times m$. Each intermediate variable in the calculation can be associated with a derivative. Exact derivatives are known for each primitive function. They are linked according to the chain rule, so that the derivative of the function output with respect to an input variable can be easily traced.

In this work, we focus on reverse-mode automatic differentiation, suitable for our typical optimization setting. For many real-world optimization tasks, the output is typically a single value, while the input comprises a considerably larger number of variables. Therefore, it is more advantageous to compute a row of the Jacobian at a time, which includes derivatives of a single output value with respect to all of the inputs. The vector Jacobian product (VJP) is defined as

$$\mathrm{VJP}(\mathbf{f}(\mathbf{v},\mathbf{x})) = \mathbf{v}^T\frac{\partial \mathbf{f}}{\partial \mathbf{x}}(\mathbf{x}), \tag{5}$$

where $\frac{\partial \mathbf{f}}{\partial \mathbf{x}}$ is the Jacobian specified above and $\mathbf{v}(\mathbf{x})$ is a vector of incoming variables. Here, one should keep in mind that intermediate results have to be stored before starting the backward pass to evaluate the gradients. Reverse mode AD is similar to the adjoint method mentioned earlier, whereas the latter does not assume a fully automatic process, rather a derivation and embedding of the adjoint equations is required. However, even for the simplified automatic differentiation process, there are numerous pitfalls to be aware of in Ref. 58. For a detailed overview of differentiable programming, we refer the reader to a recent review.[59]

JAX is used in the current version of the code to perform automatic differentiation.[60] This approach is a combination of operator overloading, similar to PyTorch,[61] and source code transformation, which is the approach in TensorFlow.[62] JAX also provides an option to define derivatives for custom primitive functions, which was used to integrate special functions required in the T-matrix approach into the computational flow. For example, spherical Bessel and Hankel functions are not defined in JAX, so they are introduced as primitive

functions with their derivative rule manually defined. An example of a primitive function definition is provided in Appendix A.

In contrast to the original package *treams*, the core functions are modified because the underlying implementation in Cython is not supported directly in the JAX framework and they have to be transformed into Python functions. We avoid Python loops, which can introduce computational bottlenecks, opting instead for vectorized operations, where it is reasonable. The test functions were computed with the original package and the current code to ensure the different implementations do not introduce numerical discrepancies. In the supplementary material (Sec. S1), we verify the gradients computed with automatic differentiation by comparison with central finite differences over a range of step sizes. Generally, gradient checks can be performed conveniently using the `check_grads` utility of JAX. Finally, while JAX uses single precision by default, we use double precision throughout optimizations to ensure higher numerical accuracy.

III. OPTIMIZATION RESULTS

The final computational tools are made publicly available.[63] To demonstrate the general applicability of our approach and ensure consistency, we present two examples from the field of Kerker-physics that highlight its strengths. These examples are intended to be illustrative, and the methodology can be applied to a wide range of other problems. We begin with an example where we inversely design a finite cluster of scatterers, in order to optimize its integrated forward-to-backward scattering ratio. It is followed by an example where a unit cell of a metasurface, consisting of multiple scatterers, is optimized, maximizing its reflectance for a specified polarization.

To evaluate our gradient-based approach against a gradient-free optimization technique, we performed optimizations using scalable constrained Bayesian optimization and included the relevant information in the supplementary material (Sec. S3) for the first example. Across the hyperparameter sweep and initial randomizations tested, we achieved, at most, half of the performance of our approach. In addition, we used the setup of the second example and performed one gradient-based optimization iteration using the FDTD solver Tidy3D and the FEM solver JCMsuite this time for the forward simulation and gradient computation, as described in the same section of the supplementary material. This comparison further demonstrates that the semi-analytical method indeed provides a computational speedup.

A. Finite cluster

If the electric and magnetic dipole responses of a scatterer have equal strength and are in phase at a given wavelength, zero dipolar backward scattering (first Kerker condition) is achieved. If they have opposite phase shift, near-zero dipolar forward scattering (second Kerker condition) takes place.[64] According to the generalized Kerker effect,[65,66] higher-order multipoles can be leveraged to achieve zero total backscattering. This, in essence, requires the constructive interference of all scattering contributions from all multipolar orders in the forward direction. In contrast, they destructively interfere in the backward direction. Even more intricate patterns emerge when specific combinations of multipoles are engineered.[67,68] Generally, an object with a scattering cross section exceeding the single-channel regime is called a superscatterer.[69–71]

In this work, we consider scattering integrated over the entire forward and backward hemispheres rather than at a single direction. Hemispherical (2π) integration is shown to deliver major advantages over single-angle detection, especially for highly anisotropic nanostructures that scatter light into sharp forward or backward lobes. Experimental studies demonstrate that relying on direct or limited-angle measurements can introduce errors of 10% or more, often underestimating or misrepresenting total scattered power.[72–74] Only 2π integration supports accurate modeling and optimization, crucial for applications such as light-trapping and absorption in solar cells.[73,75,76]

For these reasons, the objective is defined as

$$\mathrm{FOM} = \frac{\int_{S_f} |E_{\mathrm{sca}}|^2 \, \mathrm{d}S}{\int_{S_b} |E_{\mathrm{sca}}|^2 \, \mathrm{d}S}, \tag{6}$$

where E_{sca} denotes the scattered field, and S_f and S_b are the surfaces of the forward and backward hemispheres, respectively. The integrations are performed in the far field. The integrals are evaluated using a discrete quadrature method. We maximize the F/B scattering ratio from a cluster of particles consisting of a finite number of spheres of a given material. The relative position of the spheres and their size are subject to optimization. Computations employ a local basis for each T-matrix without expanding in a global basis. However, for a later discussion of the multipolar contributions to the scattering response of the entire cluster, we resort to a global basis.

To ensure all optimization problems comply with the necessary constraints, we incorporate them using a nonlinear optimizer. We opt for the method of moving asymptotes (MMA)[77] as it handles both bounds and nonlinear constraints. The constraints must be differentiable and evaluated at each iteration. The algorithm builds a sequence of convex and separable approximations to both the objective and the nonlinear constraints. We impose the no-overlap condition of adjacent spheres as a nonlinear constraint on the positions of the spheres for both finite and infinite arrangements. This is implemented by evaluating for all sphere pairs the quantity,

$$r_i + r_j - d_{ij} + s,$$

where r_i and r_j are the particle radii, $d_{ij} = \|\mathbf{x}_i - \mathbf{x}_j\|_2$ is the Euclidean distance, and $s \geq 0$ is an optional safety margin. The constraint value is taken as the maximum of this quantity over all pairs and requiring it to remain non-positive guarantees non-overlap. In addition to enforcing physical non-overlap, this constraint also serves as a numerical safeguard by preventing configurations, for which the translation coupling terms and thus the corresponding multiscattering linear system given in Eq. (4) may become poorly conditioned. In the implementation, the linear system is evaluated numerically using direct dense solve rather than by forming an inverse operator.

In addition, bound constraints specify the maximum and minimum values for the design variables, ensuring the objective is not evaluated outside permissible limits. Bounds are set on the minimum radii of the spheres to adhere to possible fabrication constraints. Another potential issue for very small spheres is the significance of quantum effects, which must be accounted for with

appropriate approximations. Consequently, we enforce a minimum radius of 5 nm.

For a physically accurate simulation, the maximum radius of the spheres and the minimal distance between them must be consistent with the number of multipoles used. This is ensured by comparing the results against simulations using a higher number of multipoles. For these reasons, we do not restrict the radii to an upper limit. In principle, it is possible to adapt the number of multipoles on the fly based on the current size parameters, but this option was not chosen here. Meanwhile, changing the number of spheres would modify the number of parameters. Therefore, it is not supported within a single run. Furthermore, since the local basis formalism is used, it is also not necessary to control whether the distance between spheres becomes too large, which would require more multipole orders in the global basis expansion than what was sufficient in the initial arrangement. With a local basis, we include up to octupole order throughout the optimizations.

The optimization results are presented in Fig. 1. Spheres with a relative permittivity of 6.25 in vacuum are initially arranged along a circle with a radius of 400 nm. This arrangement is depicted with red spheres in Fig. 1(b). In the chosen example, we have opted to consider six spheres with a radius of 80 nm. Similar results were obtained with a larger or smaller number of spheres with different radii as initial conditions. However, if the number is too large, it overly constrains the optimization search space and the performance degrades. The initial arrangement should be set on a larger circle to provide sufficient design freedom. Additional results for extended initial configurations, including cases with added outer rings, as well as the corresponding scaling of the end-to-end optimization time and the achieved normalized objective function, are provided in Sec. S2 of the supplementary material for completeness.

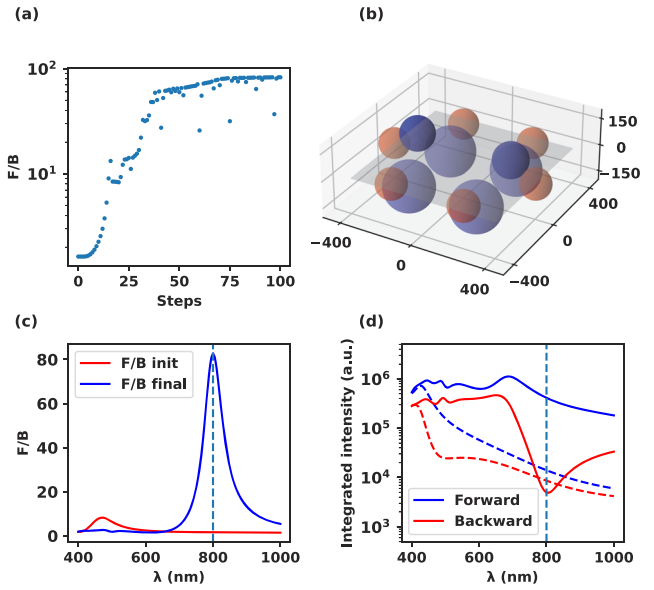

FIG. 1. (a) Convergence of the F/B ratio during optimization at the design wavelength of 800 nm when optimizing the sample from a given initial configuration, as explained in the main text. (b) 3D view of the cluster, with the z = 0 plane shown in gray and spheres on the plane rendered with lower transparency. The initial configuration is indicated in red, and the optimized structure in blue. (c) F/B ratio spectrum shows an enhancement at the design wavelength. (d) The scattered field intensity integrated over the forward (blue) and backward (red) hemispheres. The dashed curves indicate the initial arrangement and the solid curves denote the optimized one. The dashed vertical line marks the design wavelength.

To set a baseline, we initially computed the F/B scattering ratio of this given structure upon illumination with a y-polarized plane wave propagating in the z-direction in the wavelength range from 400 to 1000 nm. The F/B scattering ratio of this initial configuration is shown in Fig. 1(c). A clear peak of 10 is observed at around 450 nm, which can be attributed to the single particle magnetic dipole resonance.

Optimization of the F/B scattering ratio is performed at the design wavelength of 800 nm. The optimization variables are the 3D positions and radii of the spheres, which gives us $4N = 24$ design parameters. The number of spheres N and the multipole truncation $l_{\max}$ are fixed during an optimization run. The positions and radii of the spheres are adjusted in each iteration, respecting the overlap constraints. We initialize the spheres with small radii to avoid early overlap constraint violations during optimization. As can be seen in Fig. 1(c), the final F/B ratio reaches 80 at the design wavelength. The separately plotted numerator and denominator shown in Fig. 1(d) demonstrate that the stronger increase in the forward-scattering contribution is responsible for the increase in the total scattering. Figure 1(a) shows that the algorithm has converged after 40 iterations, where the achievable F/B scattering ratio reaches a plateau.

The optimized structure exhibits a pattern obtained in alternative optimizations with other initial arrangements as well, with some spheres shifted along the z-direction. Generally, it is observed that the spheres move closer to each other and increase in size. The initial arrangement is sixfold symmetric. However, the illumination breaks the symmetry for the gradients, except for the mirror symmetry. For this reason, the final arrangement also possesses this symmetry. However, since the target scattering pattern is not symmetric about the z axis, the optimized structure necessarily breaks the initial 6– fold rotational symmetry by introducing unequal displacements along z. The total scattering is also increased, as expected, given the larger sphere sizes in the final arrangement.

To illustrate the changes, the radiation pattern and multipole decomposition for the initial and final arrangements at the design wavelength are shown in Fig. 2. The radiation pattern, plotted here in log scale in Figs. 2(a) and 2(b), exhibits differences between the two considered planes, particularly in the strength of the sidelobes. Both radiation patterns indicate that the higher final ratio was achieved by a reduction in backward scattering and a simultaneous increase in forward scattering.

The multipole decomposition of the scattering response at the design wavelength, shown in Figs. 2(c) and 2(d), was performed by expanding the final T-matrix about a single origin, necessitating the inclusion of higher-order multipoles, i.e., this is the response expressed in the global T-matrix. In the initial arrangement, total scattering is low and dominated by two multipolar components: magnetic quadrupole (61%) and electric octupole (30%) [Fig. 2(c)]. The increased scattering strength in the optimized structure is achieved by enhancing the contribution of individual multipoles—gradually decreasing in strength for higher orders and effectively balancing the electric and magnetic components of the

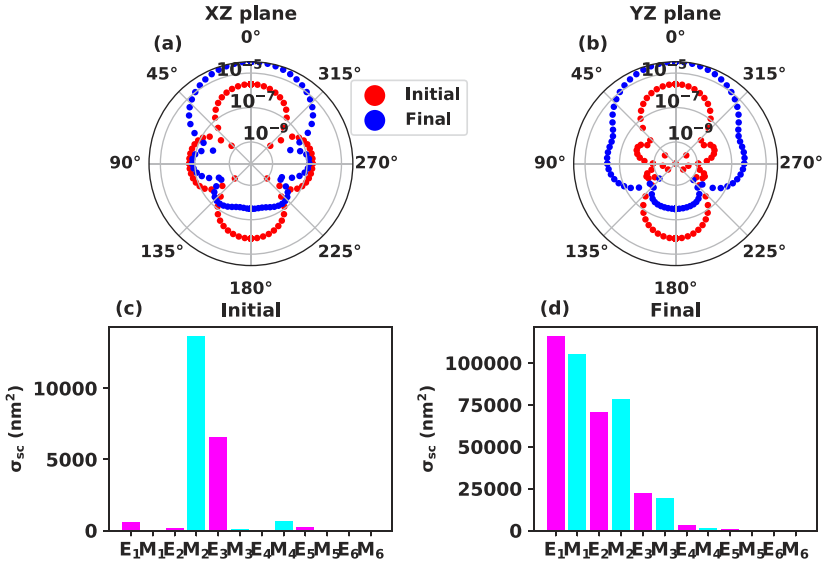

FIG. 2. Top panel: polar plots of the radiation pattern in the *XZ* (a) and *YZ* planes (b). Bottom panel: multipole contributions to the scattered cross section of the initial (c) and final arrangements (d). For visual clarity, the bars representing electric multipole contributions are represented by magenta while magnetic multipoles by cyan. All results are shown at the design wavelength.

same order (dipoles: 28% and 25.2%, quadrupoles: 17% and 18.5%, and octupoles: 5.3% and 4.5%), as shown in Fig. 2(d). The pattern is consistent with the common understanding of the Kerker effect. In particular, the different electric and magnetic multipoles contribute comparably with the total scattering response. Thanks to the suitable interference, the scattered light directly in the forward direction is two orders of magnitude larger than the light directly scattered in the backward direction. We note that, in general, equal contributions from electric and magnetic multipoles are not required.[65,66]

Finally, we verify the functionality of the designed structures in dedicated experiments. To perform the experiments, we chose microwave frequencies. This range is experimentally less demanding, while the same arrangement can, in principle, be implemented at optical frequencies, provided suitable materials and nanofabrication methods are used. To prepare the experiments, the optimization was repeated using the experimentally measured material parameters of ABS plastic, which was chosen as the material from which the spheres were made. The target wavelength was 10 cm, corresponding to a target frequency of 3 GHz. The same initial cluster arrangement was used as the starting point for the optimization, and the result of the optimization was very similar to the design introduced above. Both the initial and optimized arrangements were fabricated using 3D-printing and encapsulated in foam. The foam has electromagnetic properties close to air at the operating band and serves as a mechanical scaffold that maintains the spheres at their designed positions. With that, we can assure that the spheres are arranged as designed and structurally stable.

The electromagnetic scattering responses of the clusters were measured in the direct forward and backward directions, with the results shown in Fig. 3(c). The simulation results with CST Studio Suite are demonstrated as a cross-check in Fig. 3(d). Generally, good agreement is observed, with a tremendously enhanced forward-to-backward scattering ratio of 10^2 or more at or near the design frequency. Slight deviations occur, nevertheless, between experiment and simulations. After testing the sensitivity of the response to uncertainties in some selected parameters, we attribute the small frequency shift and larger value of the observed scattering ratio peak to minor uncertainties in the positions of the spheres, rather than to inconsistencies in the material properties. Further details of the experimental realization, along with more measurement results and a sensitivity analysis, are provided in the supplementary material. Nevertheless, we can conclude from these experiments that the inverse designs that we provide can be translated into tangible technology.

B. Metasurface with a complex unit cell

Next, as a second example, we discuss the inverse design of a metasurface that consists of a periodic arrangement with a complex unit cell. Each unit cell contains five spheres. Our purpose is to achieve a strongly polarization-dependent reflection. As discussed previously,[78] the optical response of individual scatterers is modified by the lattice interaction, and the overlap of multipole contributions with different parities can cancel light propagation in one direction. Now, if the unit cell breaks fourfold symmetry, it is possible to achieve this cancellation effect for only one of the polarizations of the incident plane wave.

The objective function is defined as

$$\mathrm{FOM} = |R_y - R_x|, \tag{7}$$

where R denotes the total reflectance, and the subscript indicates the x- or y-polarization of the incident light.

Clearly, when setting the initial arrangement, the symmetries can be broken or preserved. We choose an odd number of spheres, five in total, and position them in a circle, such that one sphere lies on the x axis. This way, the unit cell is symmetric with respect to the x axis, but not to the y axis. Hence, we can expect the cancellation to occur for the x-polarized incident field.

The setup parameters include the initial radius of a single sphere and the radius of the circle along which the spheres are arranged. The example considers silicon spheres with relative

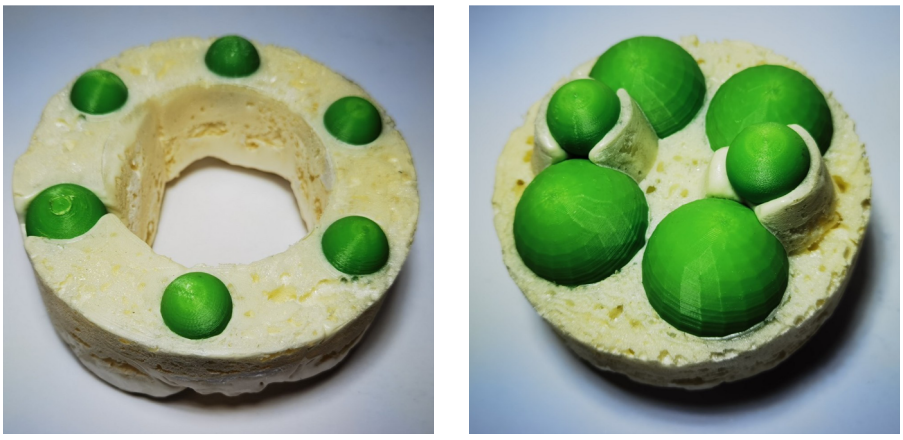

FIG. 3. Fabricated samples using 3D-printing and foam hosting: (a) the initial cluster and (b) optimized cluster. The ratio of directly forward (0°) to directly backward (180°) scattering under *y*-polarized plane wave for both structures—initial (solid blue) and optimized (solid red)—and their quotient (optimized/initial, dashed–dotted): (c) experimental measurements and (d) CST numerical simulations.

permittivity values taken from Ref. 79, embedded in a medium with a relative permittivity of 2.25. Each sphere of the initial arrangement has a radius of 10 nm, the radius of the circle is set to 170 nm, and the pitch is 600 nm. The small size of the initial spheres is chosen to ensure ample free space for the scatterers to move and grow during the optimization process. The design wavelengths selected in the following exceed the unit cell size, ensuring operation within the non-diffractive regime. The incident field is always a plane wave propagating along the *z* axis (normal incidence) and it is either *x*- or *y*-polarized.

To tune the resonance, we leave the radii and positions of the independent scatterers in the unit cell as free parameters while keeping the lattice constant fixed in the optimization. This corresponds to $4N = 20$ parameters. The spheres are not allowed to overlap and shrink below 5 nm, as in the previous example. The no-overlap condition was modified to enforce an additional minimal separation of 5 nm between spheres, based on the observation that they tend to approach each other at subnanometer distances. An additional constraint restricts the position of the spheres within the circumscribing sphere of the unit cell since the T-matrix of the arrangement in the unit cell is expanded about a common origin. Multipole contributions up to 7th order are included during optimization, and the final arrangements are recalculated up to 15th order. The splitting parameter η in the Ewald summation is selected automatically using a `treams` routine based on the wavenumber and lattice constant, and for our setup, the values are 0.42 and 0.46 for 950 and 1050 nm wavelengths, respectively. All optimizations run for up to 250 iterations and reach convergence within this number of steps.

From optimization at different wavelengths, we note that the optimizer can reach the high reflectance value for many wavelengths within a particular wavelength range, and we demonstrate the optimization results obtained at 950 and 1050 nm in Figs. 4(a), 4(b), and 4(d)–4(f).

To explore a more challenging design, we also focus on achieving dual-band performance. It is realized by applying an adaptive weighting scheme to balance the optical response at two wavelengths. The objective is defined as follows:

$$f_i = |R_y(\lambda_i) - R_x(\lambda_i)|, \quad i = 1, 2, \tag{8}$$

$$\mathrm{FOM} = \frac{2 f_1 f_2 + \varepsilon \min(f_1, f_2)}{f_1 + f_2 + \varepsilon}, \tag{9}$$

where ε is a small regularization parameter. The regularization ensures the term with the smaller value is given greater

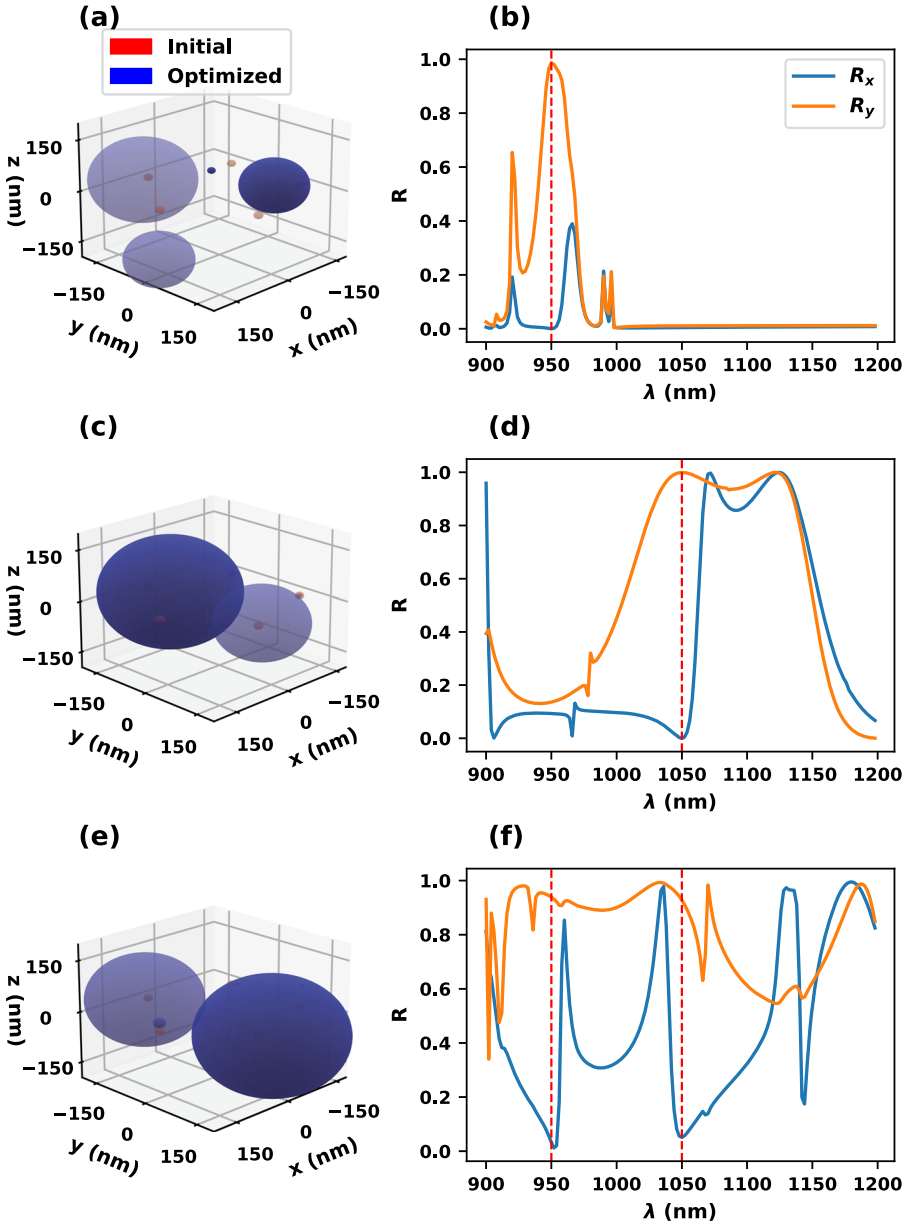

FIG. 4. Initial (red) and optimized (blue) constituents of the metasurface unit cell targeting reflection peak for one linear polarization of the incident light and a low reflection for the other one at (a) 950 nm, (b) 1050 nm, and (c) simultaneously 950 and 1050 nm. The transparency of each sphere decreases with its proximity to the viewer. Panels (d)–(f) show corresponding reflection spectra for *x*-polarized (blue curves) and *y*-polarized (orange curves) incident light. The vertical red dashed lines indicate the target wavelength(s).

emphasis. It can be observed in Fig. 4(f) that for the incident plane wave with *x*-polarization, sharp peaks are produced, while a plane wave with *y*-polarization is responsible for the wide resonance curve in reflectance.

For all optimizations, we observe that the number of spheres is effectively reduced, as the significant response is obtained only from two to three spheres that have increased considerably in size. This is to be expected, given the limited space available during optimization. Optimizations that omit the shrunken spheres from the initial configuration reproduce the same final arrangement.

To investigate the underlying behavior of the T-matrix, the phasor diagrams of the contributions of different multipoles to the components of the complex reflection coefficient are shown in Fig. 5 for the single wavelength optimized geometries, and in Fig. 6 for the dual-wavelength optimized geometry. We work with T-matrices that already include lattice interactions. As the coefficients that contribute to the backward-propagating field are needed, we switch to plane-wave basis quantities for clarity.

In Appendix B, exact formulas are provided to compute the expansion coefficient in a plane wave basis knowing the expansion coefficients in the spherical wave basis, which involve a summation procedure over all orders *l* and *m*. Rather than performing the entire summation at once, we separate the sum over particular multipole orders and polarizations and then derive the corresponding partial

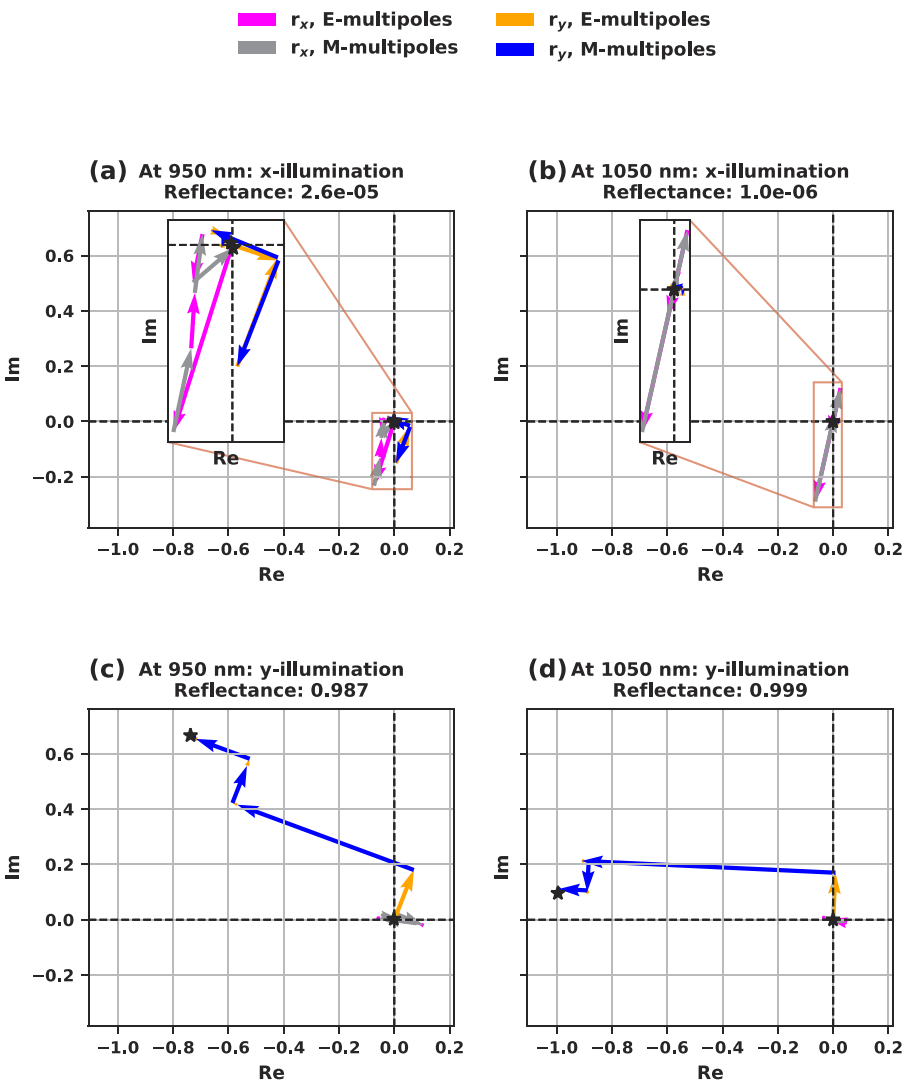

FIG. 5. Phasor diagrams of contributions of electric and magnetic multipoles to the backward-scattered field coefficients. Panels (a) and (c) show the results for a non-diffractive metasurface optimized at 950 nm, while panels (b) and (d) demonstrate the results of optimization at 1050 nm. Starting from 0, the vectors build up as E_1, M_1, E_2, M_2, and so on, where E stands for electric and M for magnetic multipoles, followed by the multipole order. Each panel shows the phasor build-up of x- and y-polarized scattered field components separately. However, the cross-polarized components are negligible. For both optimized structures illuminated with x-polarized light, in panels (a) and (b), the electric and magnetic multipole contributions cancel each other, whereas in panels (c) and (d), under y-illumination, they sum up to a high value of reflectance.

S-matrices, each accounting only for electric dipole, magnetic dipole, and so on. Next, the complex-valued reflection coefficients are calculated by multiplying the $S_{\downarrow\uparrow}$ block, with the vector representing the expansion coefficients of the plane wave, which contains one and zero according to the polarization. The final reflectance is

$$R = \left| \sum_{i=1}^{N} r_i \right|^2, \tag{10}$$

where $N = 2l_{\max}$. The reflection coefficients corresponding to each multipole with a definite total angular momentum and parity are depicted as phasors and their vector sum is the total reflection coefficient. Although the expansion includes 15 multipole orders, the phasor diagram shows that only up to octupole order contributions are significant.

In Fig. 5, the electric and magnetic multipoles cancel each other almost perfectly under x-polarized light. For y-illumination, the contributions add up to nearly perfect reflectance. The cross-polarized terms are negligible. Meanwhile, for dual-wavelength optimization shown in Fig. 6, the situation is not the same. We observe a few strong multipole contributions under y-polarized illumination that are not compensated, as expected. For the x-polarized incident field, there are components of smaller magnitudes, with some of the phasors directed in opposite directions. However, there is no explicit pairwise cancellation characteristic of the Kerker effect. In both illumination scenarios, the cross-polarized field components are non-zero and of similar magnitude, indicating that this can be disregarded when seeking the actual reason for the difference in outcomes. Clearly, the dual-band objective is more complicated to satisfy, and one cannot achieve total cancellation; however, the optimization procedure found a sufficiently close solution, and the reflectance for x-polarized light can be considered negligible.

The demonstrated results reinforce the conclusion that gradient-based methods are a powerful tool for optimization. As

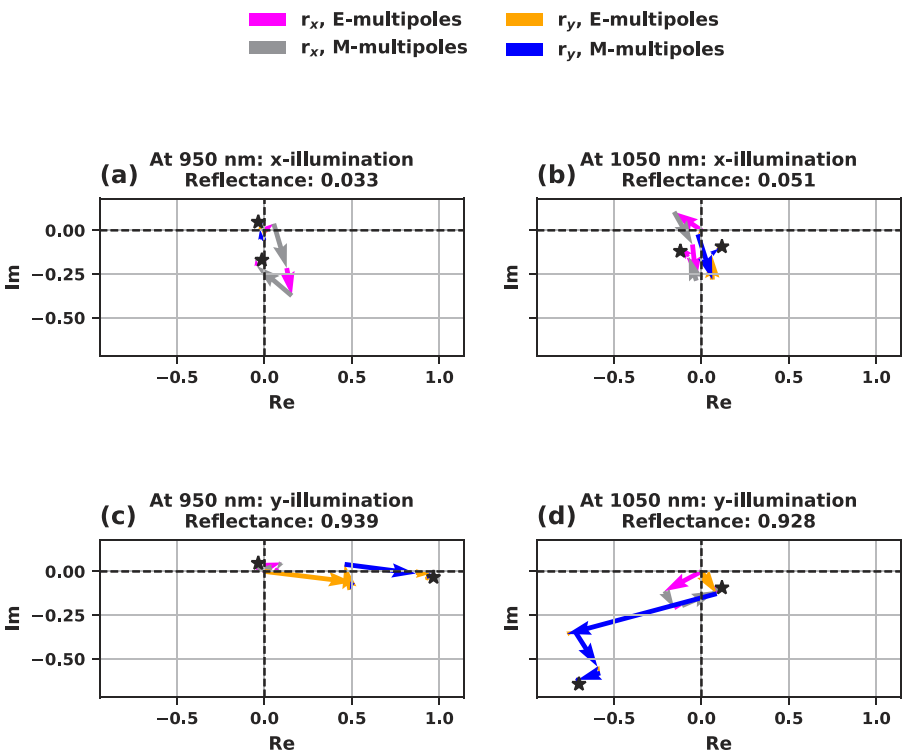

FIG. 6. Phasor diagram of contributions of electric and magnetic multipoles to the complex reflection coefficient. The non-diffractive metasurface was optimized for maximum reflectance contrast at simultaneously 950 and 1050 nm. Panels (a) and (b) demonstrate the contributions of multipoles to the complex reflection coefficient for *x*- and *y*-components of the scattered field, when the metasurface is illuminated by *x*-polarized plane wave, which results in minimal final reflectance. In panels (c) and (d), the incident plane wave is *y*-polarized, and the final reflectance is high. Each panel shows the phasor build-up of *x*- and *y*-polarized scattered field components separately.

for all local optimization techniques, the achievable results can be sensitive to the choice of initial conditions. Common approaches for avoiding convergence to suboptimal local maxima include combining these techniques with global optimization methods or performing multiple runs with varied initial conditions. Nevertheless, the gradient-based framework is essential for fine-tuning design parameters.

IV. CONCLUSION

We have developed and evaluated a differentiable computational framework for the inverse design of nanophotonic systems using the T-matrix method. The Python code is available under the MIT license (https://github.com/tfp-photonics/dreams). We applied this framework to design various structures consisting of elaborate arrangements of spherical scatterers in finite clusters and on periodic lattices. A key strength of our framework is its ability to simultaneously optimize the positions and radii of spheres, leveraging strong multipolar interactions. This capability extends directly to the positions of arbitrarily shaped scatterers, and the method can be used together with other differentiable solvers to compute derivatives with respect to any geometrical parameter. The required derivatives are efficiently obtained through automatic differentiation. Even a moderate number of parameters generate ample design space, making brute-force parameter sweeps and some global optimization techniques infeasible.

In particular, we demonstrate a maximized forward-to-backward scattering ratio for a cluster of spheres and a tailored polarization-dependent reflectance for a metasurface with a complex unit cell. Both case studies involve the cancellation of scattered fields in a specific direction, exemplifying the generalized Kerker effect. The comprehensive T-matrix approach easily reveals the contribution of different multipoles to the optimized scattered field. We ensure the simulation method itself does not impose restrictions on the inclusion of higher-order multipolar components in the optical response. From the optimization curves, we observe that the optimizations start from comparatively low initial values and converge to high-performance solutions that respect all constraints. Combining multiple objectives, as seen in the example of dual-wavelength optimization, achieves the desired functionality, even if it does not strictly follow the expected underlying mechanism. This further enhances the flexibility of the design framework.

This work opens new possibilities for the automated, high-fidelity design of complex nanophotonic architectures where multipolar interference plays a central role. By integrating differentiable programming with the T-matrix formalism, it lays the groundwork for scalable, mechanism-agnostic optimization across diverse application domains, from directional scattering to metasurface engineering. The framework is well-positioned to accelerate the inverse design of functional photonic systems beyond traditional heuristic-guided approaches.

Finally, we wish to add that at the time of the submission, we became aware of a manuscript developing similar ideas.[80] This underpins the timeliness and importance of the differentiable formulation of algorithms that solve multiple-scattering problems, a key requirement for inverse design of photonic nanostructures.

SUPPLEMENTARY MATERIAL

The supplementary material presents gradient validation and scaling analysis in terms of scatterer number and multipolar order. It also compares the approach with gradient-free optimization and gradient-based optimization iterations using full-wave solvers and describes the microwave experiments, including sample fabrication, characterization techniques, and sensitivity analysis.

ACKNOWLEDGMENTS

N.A. and C.R. acknowledge financial support from the Federal Ministry of Research, Technology, and Space (BMFTR) within the project DAPHONA (Grant No. 16DKWN039). J.D.F. and C.R. acknowledge financial support from the Helmholtz Association in the framework of the innovation platform "Solar TAP." O.K. and C.R. acknowledge support from the German Research Foundation within the Excellence Cluster 3D Matter Made to Order (EXC 2082/2 under Project No. 390761711) and from the Carl Zeiss Foundation. N.A. acknowledges support from the Max Planck School of Photonics (MPSP). N.A. and J.D.F. acknowledge support from the Karlsruhe School of Optics and Photonics (KSOP). The work of D.V. was supported by the 1.1.1.9 Activity "Post-doctoral Research" under Research Application No. 1.1.1.9/LZP/1/24/166 "Linear Industrial Monitoring System based on Hyperspectral Cameras and AI Algorithms (LIF-HYCAI)." TAU Team acknowledges the Israel Science Foundation (ISF Grant No. 1115/23). We acknowledge support by the KIT-Publication Fund of the Karlsruhe Institute of Technology.

AUTHOR DECLARATIONS

Conflict of Interest

The authors have no conflicts to disclose.

Author Contributions

N. Asadova: Conceptualization (equal); Formal analysis (lead); Investigation (equal); Methodology (equal); Software (lead); Validation (equal); Visualization (lead); Writing – original draft (lead); Writing – review & editing (equal). **J. D. Fischbach**: Investigation (equal); Methodology (equal); Software (supporting); Validation (equal); Writing – review & editing (equal). **O. Kuster**: Investigation (equal); Methodology (equal); Software (supporting); Writing – review & editing (equal). **Y. Augenstein**: Investigation (equal); Methodology (equal); Supervision (equal); Writing – review & editing (equal). **D. Vovchuk**: Formal analysis (equal); Investigation (equal); Methodology (equal); Visualization (supporting); Writing – original draft (supporting); Writing – review & editing (equal). **A. Kharchevskii**: Investigation (equal); Methodology (equal); Writing – review & editing (equal). **P. Ginzburg**: Funding acquisition (equal); Investigation (equal); Methodology (equal); Project administration (supporting); Supervision (equal); Writing – review & editing (equal). **C. Rockstuhl**: Conceptualization (equal); Funding acquisition (equal); Investigation (equal); Methodology (equal); Project administration (lead); Supervision (lead); Writing – review & editing (equal).

DATA AVAILABILITY

The data that support the findings of this study are openly available at Ref. 63.

APPENDIX A: CUSTOM DERIVATIVE

The derivative of the spherical Bessel (and Hankel) functions is calculated using the recurrence relation. The special case of zero argument has to be treated accordingly. For $\nu > 1$, it can be set to zero, while for $\nu = 1$, the Taylor series expansion of *sinc* gives a non-zero number. The code snippet is provided in LISTING 1.

APPENDIX B: TRANSLATION FROM PERIODIC VECTOR SPHERICAL WAVE COEFFICIENTS TO PLANE WAVE COEFFICIENTS

The scattered field summed over the periodic lattice in the plane wave basis can be written as follows:

$$\mathbf{E}_{\mathrm{scat}}^{(\mathrm{lattice}),\,d}(\mathbf{r}) = \sum_{g\in\Lambda^*} e^{\,i(\mathbf{k}_\parallel+g)\cdot\mathbf{r}}\big[C_{\mathrm{TE}}(g)\;\hat{e}_{\mathrm{TE}}(\mathbf{k}_\parallel+g,\;d) + C_{\mathrm{TM}}(g)\;\hat{e}_{\mathrm{TM}}(\mathbf{k}_\parallel+g,\;d)\big]. \tag{B1}$$

LISTING 1. Example: custom spherical Bessel function in JAX.

```
def spherical_jn(v, z):
    z = z.astype(np.result_type(complex,
        z.dtype))
    return jax.pure_callback(
       lambda v, z: mod_jn(v, z).astype(z.
        z.dtype),
       jax.ShapeDtypeStruct(
       shape=np.broadcast_shapes(v
         .shape, z.shape),
       dtype=z.dtype
       ),
       v, z,
       vmap_method="legacy_vectorized"
    )
@spherical_jn.defjvp
def _jv_jvp(primals, tangents):
    """
    Custom JVP rule for spherical Bessel
      function.
    """
    v, z = primals
    _, z_dot = tangents # v_dot = 0 since
       v is integer.
    jv_v_z = spherical_jn(v, z)
    jv_plus_1 = spherical_jn(v + 1, z)
    small_z = np.abs(z) < 1e-8
    djv_dz = np.where(
    (small_z & (v != 1)), 0.0j,
    np.where(
      (small_z & (v == 1)), 1/3,
      v * jv_v_z / z - jv_plus_1
    )
  )
return jv_v_z, z_dot * djv_dz
```

In the expression above, $\mathbf{k}_\parallel$ is the tangential component of the plane wave and g is the diffraction order. The expansion coefficients are given by

$$\begin{pmatrix} C_{\mathrm{TE}}(g) \\ C_{\mathrm{TM}}(g) \end{pmatrix} = \sum_{\ell=1}^{\ell_{\max}} \sum_{m=-\ell}^{\ell} F_{\ell m}(g) \underbrace{\begin{pmatrix} \tau_{\ell m}(\theta_g) & \pi_{\ell m}(\theta_g) \\ \pi_{\ell m}(\theta_g) & \tau_{\ell m}(\theta_g) \end{pmatrix}}_{A_{\ell m}(\theta_g)} \begin{pmatrix} p_{e,\ell m} \\ p_{m,\ell m} \end{pmatrix}, \tag{B2}$$

where $\pi_{\ell m}(\theta_g)$ and $\tau_{\ell m}(\theta_g)$ are the two angle-dependent functions defined in terms of the associated Legendre functions P_l^m,

$$\pi_{lm}(\theta) = \frac{m}{\sin\theta} P_l^m(\cos\theta), \qquad \tau_{lm}(\theta) = \frac{d}{d\theta} P_l^m(\cos\theta). \tag{B3}$$

Finally,

$$F_{\ell m}(g) = -\frac{i\pi N_{\ell m}}{a\, k\, i^{\ell-m}} \frac{1}{\sqrt{1 - |\mathbf{k}_\parallel + g|^2/k^2}}, \qquad \cos\theta_g = \frac{\sqrt{k^2 - |\mathbf{k}_\parallel + g|^2}}{k}, \tag{B4}$$

where $N_{\ell m}$ is the normalization constant of the VSW and a is the area of the unit cell.

REFERENCES

[1] S. Molesky, Z. Lin, A. Y. Piggott, W. Jin, J. Vucković, and A. W. Rodriguez, Nat. Photonics **12**, 659 (2018).
[2] S. D. Campbell, D. Sell, R. P. Jenkins, E. B. Whiting, J. A. Fan, and D. H. Werner, Opt. Mater. Express **9**, 1842 (2019).
[3] K. Yao, R. Unni, and Y. Zheng, Nanophotonics **8**, 339 (2019).
[4] Q. Wang, M. Makarenko, A. Burguete Lopez, F. Getman, and A. Fratalocchi, Nanophotonics **11**, 2483 (2022).
[5] P. Bennet, D. Langevin, C. Essoual, A. Khaireh-Walieh, O. Teytaud, P. Wiecha, and A. Moreau, J. Opt. Soc. Am. B **41**, A126 (2024).
[6] P. R. Wiecha, A. Arbouet, C. Girard, and O. L. Muskens, Photonics Res. **9**, B182 (2021).
[7] T. Ma, M. Tobah, H. Wang, and L. J. Guo, Opto-Electron. Sci. **1**, 210012 (2022).
[8] D. Sell, J. Yang, S. Doshay, R. Yang, and J. A. Fan, Nano Lett. **17**, 3752 (2017).
[9] Z. Lin, V. Liu, R. Pestourie, and S. G. Johnson, Opt. Express **27**, 15765 (2019).
[10] S. Stich, J. Mohajan, D. de Ceglia, L. Carletti, H. Jung, N. Karl, I. Brener, A. W. Rodriguez, M. A. Belkin, and R. Sarma, ACS Nano **19**, 17374 (2025).
[11] A. Mirzaei, A. E. Miroshnichenko, I. V. Shadrivov, and Y. S. Kivshar, Sci. Rep. **5**, 9574 (2015).
[12] Z. Li, L. Stan, D. A. Czaplewski, X. Yang, and J. Gao, Opt. Lett. **44**, 114 (2018).
[13] P. R. Wiecha, C. Majorel, C. Girard, A. Cuche, V. Paillard, O. L. Muskens, and A. Arbouet, Opt. Express **27**, 29069 (2019).
[14] P.-I. Schneider, X. G. Santiago, C. Rockstuhl, and S. Burger, Proc. SPIE **10335**, 103350O (2017).
[15] P. R. Wray, E. G. Paul, and H. A. Atwater, Nanophotonics **13**, 183 (2024).
[16] K. Eggensperger, M. Feurer, F. Hutter, J. Bergstra, J. Snoek, H. Hoos, K. Leyton-Brown *et al.*, in *NIPS Workshop on Bayesian Optimization in Theory and Practice* (2013), Vol. 10, pp, 1–5.
[17] G. Angeris, J. Vučković, and S. Boyd, Opt. Express **29**, 2827 (2021).
[18] S. D. Campbell, D. Sell, R. P. Jenkins, E. B. Whiting, J. A. Fan, and D. H. Werner, "Review of numerical optimization techniques for meta-device design," Opt. Mater. Express **9**, 1842–1863 (2019).
[19] J. Jiang, M. Chen, and J. A. Fan, Nat. Rev. Mater. **6**, 679 (2021).
[20] Z. Li, R. Pestourie, Z. Lin, S. G. Johnson, and F. Capasso, ACS Photonics **9**, 2178 (2022).
[21] S. Molesky, P. Chao, J. Mohajan, W. Reinhart, H. Chi, and A. W. Rodriguez, Phys. Rev. Res. **4**, 013020 (2022).
[22] P. Chao, B. Strekha, R. Kuate Defo, S. Molesky, and A. W. Rodriguez, Nat. Rev. Phys. **4**, 543 (2022).
[23] M. P. Bendsoe and O. Sigmund, *Topology Optimization: Theory, Methods, and Applications* (Springer Science & Business Media, 2013).
[24] A. Y. Piggott, J. Petykiewicz, L. Su, and J. Vučković, Sci. Rep. **7**, 1786 (2017).
[25] Y. Augenstein and C. Rockstuhl, ACS Photonics **7**, 2190 (2020).
[26] A. M. Hammond, A. Oskooi, S. G. Johnson, and S. E. Ralph, Opt. Express **29**, 23916 (2021).
[27] A. Luce, R. Alaee, F. Knorr, and F. Marquardt, Mach. Learn.: Sci. Technol. **5**, 025076 (2024).
[28] T. W. Hughes, I. A. D. Williamson, M. Minkov, and S. Fan, ACS Photonics **6**, 3010 (2019).
[29] S. Hooten, P. Sun, L. Gantz, M. Fiorentino, R. Beausoleil, and T. Van Vaerenbergh, Laser Photonics Rev. **19**, 2301199 (2025).
[30] B. Vial and Y. Hao, Mathematics **10**, 3912 (2022).
[31] T. Xue, S. Liao, Z. Gan, C. Park, X. Xie, W. K. Liu, and J. Cao, Comput. Phys. Commun. **291**, 108802 (2023).
[32] V. Liu and S. Fan, Comput. Phys. Commun. **183**, 2233 (2012).
[33] J. P. Hugonin and P. Lalanne, arXiv:2101.00901 (2021).
[34] S. Colburn and A. Majumdar, Commun. Phys. **4**, 65 (2021).
[35] Z. Zhu and C. Zheng, Opt. Express **28**, 37773 (2020).
[36] S. So, J. Kim, T. Badloe, C. Lee, Y. Yang, H. Kang, and J. Rho, Adv. Mater. **35**, 2208520 (2023).
[37] C. Kim and B. Lee, Comput. Phys. Commun. **282**, 108552 (2023).
[38] W. Jin, W. Li, M. Orenstein, and S. Fan, ACS Photonics **7**, 2350 (2020).
[39] A. S. Backer, Opt. Express **27**, 30308 (2019).
[40] T. Phan, D. Sell, E. W. Wang, S. Doshay, K. Edee, J. Yang, and J. A. Fan, Light: Sci. Appl. **8**, 48 (2019).
[41] J. R. Capers, S. J. Boyes, A. P. Hibbins, and S. A. R. Horsley, "Designing the collective non-local responses of metasurfaces," Commun. Phys. **4** (2021).
[42] S. Ponomareva, A. Patoux, C. Majorel, A. Azéma, A. Cuche, C. Girard, A. Arbouet, and P. Wiecha, SciPost Phys. Codebases **2025**, 60.
[43] V. Yannopapas and A. G. Vanakaras, Phys. Rev. B **84**, 085119 (2011).
[44] D. Pal and A. F. Koenderink, Laser Photonics Rev. **19**, e02199 (2025).
[45] K. Tanaka, D. Arslan, S. Fasold, M. Steinert, J. Sautter, M. Falkner, T. Pertsch, M. Decker, and I. Staude, ACS Nano **14**, 15926 (2020).
[46] G. Salerno, R. Heilmann, K. Arjas, K. Aronen, J.-P. Martikainen, and P. Törmä, Phys. Rev. Lett. **129**, 173901 (2022).
[47] D. Beutel, I. Fernandez-Corbaton, and C. Rockstuhl, Comput. Phys. Commun. **297**, 109076 (2024).
[48] A. Zhan, T. K. Fryett, S. Colburn, and A. Majumdar, Appl. Opt. **57**, 1437 (2018).
[49] A. Zhan, R. Gibson, J. Whitehead, E. Smith, J. R. Hendrickson, and A. Majumdar, Sci. Adv. **5**, eaax4769 (2019).
[50] V. Igoshin, A. Kokhanovskiy, and M. Petrov, Opt. Lett. **50**, 1735 (2025).
[51] M. Tsukerman, K. Grotov, and P. Ginzburg, arXiv:2511.05357 (2025).
[52] J. D. Fischbach, F. Betz, N. Asadova, P. Tassan, D. Urbonas, T. Stöferle, R. F. Mahrt, S. Burger, C. Rockstuhl, F. Binkowski, and T. J. Sturges, Adv. Theory Simul. **8**, 2400989 (2025).
[53] J. D. Jackson, *Classical Electrodynamics* (Wiley, 1998).
[54] O. R. Cruzan, Q. Appl. Math. **20**, 33 (1962).
[55] R. N. S. Suryadharma, M. Fruhnert, I. Fernandez-Corbaton, and C. Rockstuhl, Phys. Rev. B **96**, 045406 (2017).
[56] P. P. Ewald, Ann. Phys. **369**, 253 (1921).
[57] D. Beutel, I. Fernandez-Corbaton, and C. Rockstuhl, Phys. Rev. A **107**, 013508 (2023).
[58] J. Hückelheim, H. Menon, W. Moses, B. Christianson, P. Hovland, and L. Hascoët, WIREs Data Min. Knowl. Discovery **14**, e1555 (2024).
[59] M. Blondel and V. Roulet, arXiv:2403.14606 (2024).
[60] J. Bradbury, R. Frostig, P. Hawkins, M. J. Johnson, C. Leary, D. Maclaurin, G. Necula, A. Paszke, J. VanderPlas, S. Wanderman-Milne, and Q. Zhang (2018). "JAX: Composable transformations of Python+NumPy programs," GitHub. https://github.com/jax-ml/jax

[61] A. Paszke, S. Gross, F. Massa, A. Lerer, J. Bradbury, G. Chanan, T. Killeen, Z. Lin, N. Gimelshein, L. Antiga *et al.*, *Advances in Neural Information Processing Systems* (Advances in Neural Information Processing Systems, 2019), Vol. 32.
[62] M. Abadi, P. Barham, J. Chen, Z. Chen, A. Davis, J. Dean, M. Devin, S. Ghemawat, G. Irving, M. Isard *et al.*, in *12th USENIX Symposium on Operating Systems Design and Implementation (OSDI 16)* (USENIX Association, 2016), pp. 265–283.
[63] N. Asadova and J. D. Fischbach (2025). "Dreams: Differentiable multiscattering code," GitHub. https://github.com/tfp-photonics/dreams
[64] A. Alu and N. Engheta, J. Nanophotonics **4**, 041590 (2010).
[65] R. Alaee, R. Filter, D. Lehr, F. Lederer, and C. Rockstuhl, Opt. Lett. **40**, 2645 (2015).
[66] W. Liu and Y. S. Kivshar, Opt. Express **26**, 13085 (2018).
[67] A. E. Miroshnichenko, A. B. Evlyukhin, Y. F. Yu, R. M. Bakker, A. Chipouline, A. I. Kuznetsov, B. Luk'yanchuk, B. N. Chichkov, and Y. S. Kivshar, Nat. Commun. **6**, 8069 (2015).
[68] H. K. Shamkhi, K. V. Baryshnikova, A. Sayanskiy, P. Kapitanova, P. D. Terekhov, P. Belov, A. Karabchevsky, A. B. Evlyukhin, Y. Kivshar, and A. S. Shalin, Phys. Rev. Lett. **122**, 193905 (2019).
[69] Z. Ruan and S. Fan, Phys. Rev. Lett. **105**, 013901 (2010).
[70] R. W. Ziolkowski, Phys. Rev. X **7**, 031017 (2017).
[71] S. Krasikov, M. Odit, D. Dobrykh, I. Yusupov, A. Mikhailovskaya, D. Shakirova, A. Shcherbakov, A. Slobozhanyuk, P. Ginzburg, D. Filonov, and A. Bogdanov, Phys. Rev. Appl. **15**, 024052 (2021).
[72] T. Lindström and A. Roos, Rev. Sci. Instrum. **71**, 2270 (2000).
[73] D. N. R. Payne, M. D. B. Charlton, and D. M. Bagnall, Appl. Opt. **54**, 7224 (2015).
[74] M. Kim and W. D. Philpot, Appl. Opt. **44**, 6952 (2005).
[75] J. Jung, T. Søndergaard, T. G. Pedersen, K. Pedersen, A. N. Larsen, and B. B. Nielsen, Am. Phys. Soc. **83**, 085419 (2011).
[76] H. U. Ulriksen, T. Søndergaard, T. G. Pedersen, and K. Pedersen, Opt. Express **27**, 14308 (2019).
[77] K. Svanberg, "A class of globally convergent optimization methods based on conservative convex separable approximations," SIAM J. Optim. **12**, 555 (2002).
[78] V. E. Babicheva and A. B. Evlyukhin, Laser Photonics Rev. **11**, 1700132 (2017).
[79] C. Schinke, P. Christian Peest, J. Schmidt, R. Brendel, K. Bothe, M. R. Vogt, I. Kröger, S. Winter, A. Schirmacher, S. Lim *et al.*, AIP Adv. **5**, 067168 (2015).
[80] Oscar KC Jackson, S. De Liberato, O. L. Muskens, and P. R. Wiecha, "PyMieDiff: A differentiable Mie scattering library," APL Photonics **11**, 1 (2026).